JOURNAL OF SOLID STATE CHEMISTRY 8, 86–99 (1973)

Compounds in the System Cr_2O_3–Fe_2O_3–TiO_2–ZrO_2 Based on Intergrowth of the α-PbO_2 and V_3O_5 Structural Types

I. E. GREY AND A. F. REID

CSIRO Division of Mineral Chemistry, Port Melbourne, Victoria 3207, Australia

AND

J. G. ALLPRESS

CSIRO Division of Tribophysics, University of Melbourne, Parkville, Victoria 3052, Australia

Received November 28, 1972

For suitable Cr:Fe and Ti:Zr ratios in the system Cr_2O_3–Fe_2O_3–TiO_2–ZrO_2 the composition range $MO_{1.667}$ to MO_2 contains a quasicontinuous series of compounds whose structures are ordered intergrowths of the V_3O_5 and α-PbO_2 structural types. The stoichiometries of the intergrowth phases are described by the general formula

$$(Cr, Fe)_{2p}(Ti, Zr)_{p+2q}O_{5p+4q} \equiv pM_3O_5 \cdot qM_2O_4,$$

where p and q can take any integral values. The compounds are monoclinic, with unit cells defined by α-PbO_2 unit cell vectors such that in all cases $a \simeq 7.0$ Å, $b \simeq 5.0$ Å and $\beta = 138°$, and c is defined by the periodicity of the M_3O_5 and M_2O_4 slabs. X-Ray and electron diffraction results are consistent with a structural model in which there is a *maximum alternation* of the M_3O_5 and M_2O_4 slabs. An alternative description in terms of crystallographic shear (CS) is also possible, whereby each of the compounds may be considered to derive from rutile by CS on planes (hkl) where

$$(hkl)_r = p(121)_r + q(011)_r.$$

1. Introduction

In the system Cr_2O_3–Fe_2O_3–TiO_2 we have previously reported (*1*, *2*) the characterization of a number of compounds which are structurally related to α-PbO_2 (*3*). They include an homologous series of phases $(Cr, Fe)_2Ti_{n-2}O_{2n-1}$, $n = 3$, 4, 5, and several ordered intergrowths between adjacent homologues. The first member of the series, $(Cr_xFe_{1-x})_2TiO_5$ $(0.5 < x < 0.85)$, is isomorphous with V_3O_5 (*4*), while the structure of the second, e.g., $(Cr_{0.5}Fe_{0.5})_2Ti_2O_7$ (*2*), may be described as an ordered intergrowth of the V_3O_5 and α-PbO_2 structural types.

Controlled replacement of Ti by Zr in the system $(Cr, Fe)_2O_3$–$(Ti, Zr)O_2$ has enabled us to extend the series of phases to higher homologues ($n \leqslant 9$) and to prepare higher order intergrowths. A careful study of X-ray and electron diffraction data for these compounds has revealed that both the homologues *and* their intergrowths can be regarded as members of a single series of intergrowths of the V_3O_5 and α-PbO_2 structural types, having the general formula $pM_3O_5 \cdot qM_2O_4$ or $(Cr, Fe)_{2p}(Ti, Zr)_{p+2q}O_{5p+4q}$, where p and q are integers.

An alternative description in terms of crystallographic shear (CS) is also possible. Several of the simpler structures can in principle be derived from that of α-PbO_2 by the periodic application of a "step shear" parallel to $(110)_{\alpha\text{-}PbO_2}$ (*1*). This description has proved to be of limited value, because it does not correctly predict the structures of other members of the series. For example, the structure which was inferred for the compound $(Cr, Fe)_2Ti_3O_9$ (*1*) possesses primitive symmetry, whereas electron diffraction patterns from single-crystal fragments of this compound indicate that the monoclinic unit cell is centered.

Copyright © 1973 by Academic Press, Inc.
All rights of reproduction in any form reserved.
Printed in Great Britain

A much more successful CS description is obtained by relating the structures to that of rutile, using the classifications and idealized models developed by Bursill *et al.* (*5*). These workers showed that a great number of compounds in the systems TiO_{2-x} and $(Ti,Cr)O_{2-x}$ could be derived from rutile by a sequence of CS operations of two simple types:

a. The operation $\frac{1}{2}[0\bar{1}1]_r(011)_r$ (r = rutile) has the effect of introducing an antiphase boundary (APB) into the structure, without altering the composition. This is illustrated in Fig. 1(i), which is an idealized representation of a pseudo-hexagonal $(100)_r$ layer of oxygen ions in rutile, with the sites occupied by metal atoms drawn as filled circles.

b. The operation $\frac{1}{2}[0\bar{1}1]_r(121)_r$, shown in Fig. 1ii, is accompanied by the removal of a plane of oxygen atoms, and therefore alters the composition towards higher metal:oxygen ratios.

Repeated application of these shear operations leads to the model shown in Fig. 1(iii) and (iv), which are recognizable as idealized representations of the α-PbO_2 and V_3O_5 structural types, respectively. It is then a straightforward matter to show that *intergrowths* of these two structures, $pM_3O_5 \cdot qM_2O_4$, may also be derived from rutile by combinations of the operations shown in Fig. 1(i) and (ii). The resultant CS plane $(hkl)_r$ is given by

$$(hkl)_r = p(121)_r + q(011)_r.$$

This formula is equivalent to that derived by Bursill *et al.* (*5*) to describe families of shear structures in TiO_{2-x} and $(Ti,Cr)O_{2-x}$.

We can therefore describe the new phases in the system $(Cr,Fe)_2O_3$–$(Ti,Zr)O_2$ either as intergrowths of the α-PbO_2 and V_3O_5 structure types, or as CS structures derived from rutile. Because the former description is very easy to visualize, we have used it in this paper to present model structures for members of the family $pM_3O_5 \cdot qM_2O_4$, and we will discuss the relevant experimental data in terms of this concept. Finally, we will discuss the relationship between these structures and those of other rutile-derived CS phases.

2. Intergrowth of the V_3O_5 and α-PbO_2 structure types

An idealized model (*1*) of the structure of $CrFeTi_2O_7$ (*2*) is shown in Fig. 2(i), using the representation developed by Andersson and Galy (*6*). The projection axis is [010] with a 5 Å repeat. When the real structure is viewed down

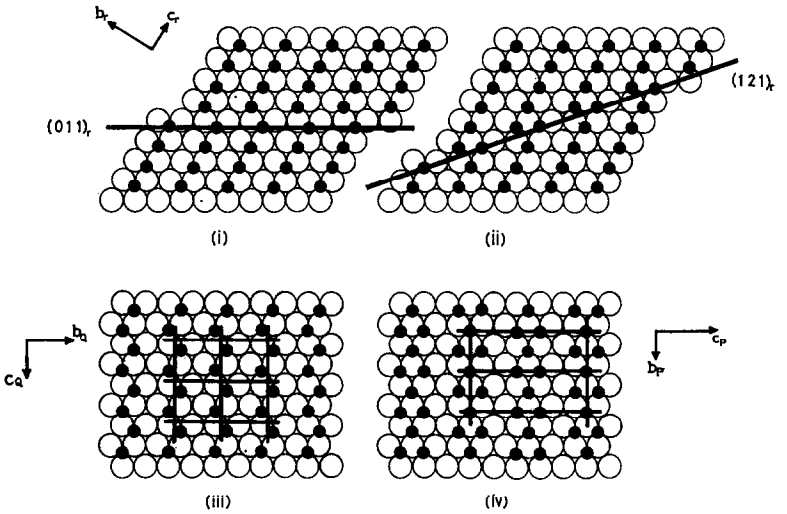

FIG. 1. Hexagonal close-packed oxygen layers corresponding to idealized $(100)_r$ planes. Small filled circles are metal atoms. (i) Result of the $\frac{1}{2}[0\bar{1}1](011)_r$ APB operation. The heavy line represents the intersection of the $(011)_r$ shear plane with $(100)_r$. (ii) Result of the $\frac{1}{2}[0\bar{1}1](121)_r$ CS operation. (iii) (100) layer of the α-PbO_2 structure, derived from rutile by repeated application of shear on $(011)_r$, operation (i). (iv) (100) layer of the V_3O_5 structure, derived from rutile by repeated application of shear on $(121)_r$, operation (ii). In (iii) and (iv) the heavy lines define the unit cells of α-PbO_2 and V_3O_5.

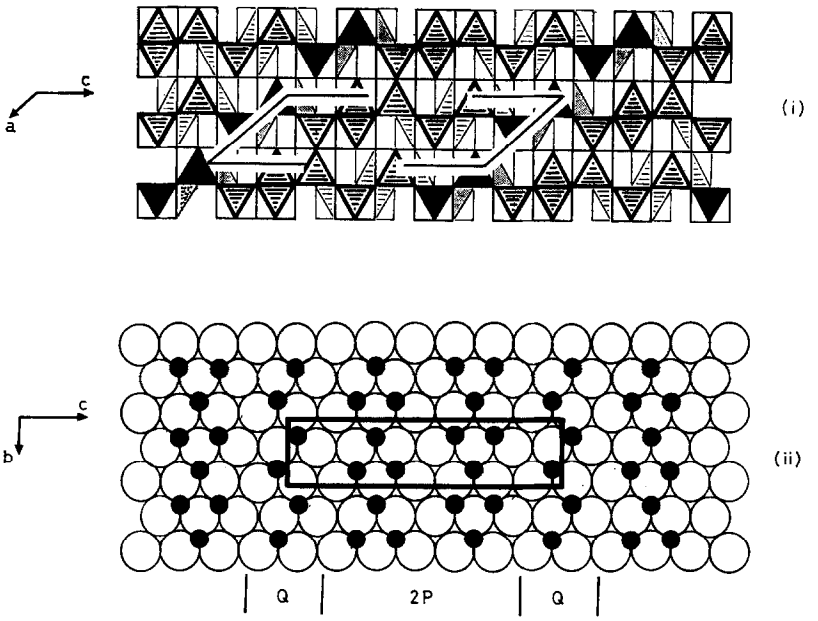

FIG. 2. Idealized representations of the structure of $(Cr,Fe)_2Ti_2O_7$. (i) [010] projection. The V_3O_5 slabs are shown with heavy horizontal hatching for metal atoms at $y = 3/4$, light hatching for $y = 1/4$; α-PbO_2 slabs are shown, blocked, for $y = 3/4$, stippled at $y = 1/4$. The unit cell (see Table I) is outlined. (ii) (100) oxygen layer in $(Cr,Fe)_2Ti_2O_7$. Small filled circles are metal atoms. The V_3O_5 and α-PbO_2 slabs are indicated by P and Q, respectively. The heavy lines define the unit cell.

[100], oxygen atoms can be seen to form pseudo-hexagonal layers and these are shown idealized in Fig. 2(ii). The correspondence with Fig. 1(iii) and (iv) is obvious, and one can immediately recognize slabs of the V_3O_5 and α-PbO_2 structure types, labelled P and Q, respectively, which are intergrown parallel to $(110)_Q$. The composition of these slabs is $P = M_3O_5$, $Q = M_2O_4$, and the compound is an ordered 2:1 intergrowth with the sequence PPQPPQPPQPP, and stoichiometry given by

$$P_2Q = 2M_3O_5 + M_2O_4 = M_8O_{14} \text{ (i.e., } 2 \times CrFeTi_2O_7).$$

Since V_3O_5 can also be described by vectors derived from the α-PbO_2 cell (*1*), it is possible to define a monoclinic unit cell for $CrFeTi_2O_7$ in which the *a*, *b*, and *c* axes lie parallel to three unique vectors in the α-PbO_2 unit cell, viz., $[110]_Q$, $[001]_Q$, and $[010]_Q$, respectively. The parameters for this unit cell, as shown in Fig. 2, are then given by $\bar{a} = \bar{a}_Q - \bar{b}_Q$; $\bar{b} = -\bar{c}_Q$; $\bar{c} = 3.5\,\bar{b}_Q$, and

$$\beta = \arctan(\bar{a}/\bar{b})_Q.$$

It is clear that a great variety of intergrowths of slabs of M_3O_5 and M_2O_4 are possible, with compositions MO_x lying between the limits $x = 1.667$ and $x = 2.000$. Their monoclinic unit cells will have constant values of *a*, *b*, and β, and the length of their *c* axis will be determined by the periodicity of the intergrowth sequence. It is easy to show that, in general, for any ordered intergrowth $pM_3O_5 \cdot qM_2O_4$, or P_pQ_q, the unit cell dimensions[1] will be given by

$$\begin{aligned} \bar{a} &= \bar{a}_Q - \bar{b}_Q, \\ \bar{b} &= -\bar{c}_Q, \\ \bar{c} &= \left(\frac{5p+4q}{m}\right)\bar{b}_Q, \text{ where } m = 4 \text{ for } p \text{ even}, \\ &\qquad\qquad\qquad\qquad\quad m = 2 \text{ for } p \text{ odd}, \\ \beta &= \arctan(\bar{a}/\bar{b})_Q. \end{aligned} \tag{1}$$

Using the cell parameters for the α-PbO_2 form of rutile, which is formed at high pressures

[1] These expressions define unit cells which differ from those previously chosen (*1*, *2*) in which both *c* and β varied for each member of the series. The new unit cells are more appropriate in the present context, because the $(100)_{rutile}$ planes correspond to the $(100)_{intergrowth}$ pseudo-hexagonal oxygen layers, shown for example in Fig. 2(ii), and the *c* axis is simply defined by the periodicity of P and Q slabs in this plane. A similar definition of unit cells in terms of unique subcell vectors has been recently suggested for the series of phases V_nO_{2n-1} (*7*).

(*8*), we obtain the following values for the dimensions of intergrowth structures:

$$a = 7.10 \text{ Å}, \simeq \sqrt{2} \times 5.00 \text{ Å},$$
$$b = 4.905 \text{ Å},$$
$$c = \left(\frac{5p + 4q}{m}\right) 5.46 \text{ Å},$$
$$\beta = 138°.$$

Although these vectorial expressions define the periodicity of the intergrowth $pM_3O_5 \cdot qM_2O_4$, they give no information concerning the sequence in which the slabs are arranged within the repeating unit. For example, if $p = 4$, $q = 3$, we could envisage the following sequences for the same composition, $M_{18}O_{32}$:

Q Q Q P P P P Q Q Q P P P P Q Q Q (i)

Q Q P P Q P P Q Q P P Q P P Q Q P (ii)

Q P Q P Q P P Q P Q P Q P P Q P Q (iii)

For compounds in the $(Cr,Fe)_2O_3$–$(Ti,Zr)O_2$ system we will show that the structural models which are most closely compatible with the observed diffraction data are those in which there is a *maximum alternation* of P and Q slabs. Thus, for the example shown above and represented by $(Cr,Fe)_8(Ti,Zr)_{10}O_{32}$, the correct sequence is (iii).

3. Experimental Methods

3.1. Preparation of Compounds

Compounds with the general stoichiometries $(Cr_xFe_{1-x})_{2p}$ $(Ti_yZr_{1-y})_{p+2q}O_{5p+4q}$ were prepared by heating finely ground pelletized mixtures of the component oxides in air or nitrogen at 1400–1700°C for periods up to 20 hr, followed by quenching to room temperature. The starting materials were Fisher Certified TiO_2 (anatase form), ZrO_2 and Fe_2O_3, together with Cr_2O_3 prepared in a reactive form by decomposing analytical grade ammonium dichromate, heated finally at 900°C for 30 min.

3.2. Homogeneity of the Preparations

Each product was examined by powder X-ray diffraction and selected area electron diffraction to determine if a single phase was present. The homogeneity of the specimens was found to be very dependent on the ratios Cr/Fe and Ti/Zr. The best results were obtained when both x and y in the general formula lay in the range 0.7–0.8. At higher chromium contents Andersson phases $Cr_2Ti_{n-2}O_{2n-1}$ (*9*) were present in the products, and at low chromium contents pseudobrookite, Fe_2TiO_5 (*10*), formed as a second phase. In the absence of zirconium we could obtain compounds only in the composition range $MO_{1.667}(M_3O_5)$ to $MO_{1.80}(M_5O_9)$ (*1*). On the other hand if the zirconium content was too high, heterogeneous products containing ZrO_2, $ZrTiO_4$, and $(Cr,Fe)_2O_3$ were obtained. The controlled replacement of titanium by zirconium ($ZrTiO_4$ being itself of α-PbO_2 type) enabled us to extend the composition range of the series to $MO_{1.89}$.

At appropriate compositions and temperatures samples were obtained whose X-ray powder diffraction patterns indicated them to be homogeneous. However, electron diffraction patterns from individual single-crystal fragments clearly showed that at the "superlattice" level there were frequent departures from strict homogeneity. Thus, while the patterns displayed the same array of strong subcell reflections, there were small differences in the number and position of weaker superlattice reflections, none of which were detectable by X-ray powder methods. In particular, spacing and orientation anomalies similar to those first described by Spyridelis, Delavignette, and Amelincky (*11*), were often observed. The structural significance of orientation anomalies will be discussed in a later paper, and for the present we will confine our attention to patterns without them.

3.3. X-Ray Diffraction

X-Ray powder patterns were obtained using a Philips diffractometer fitted with a graphite monochromator, employing Cu$K\alpha$ radiation. Potassium chloride ($a_0 = 6.2931$ Å) was used as an internal standard for lattice parameter determination, and slow scan rates were employed so as to improve precision.

3.4. Electron Diffraction

Small portions of the samples were finely ground in an agate mortar, dispersed in an inert liquid (methyl chloroform), and collected on carbon-coated specimen grids. They were examined in electron microscopes which were equipped with goniometer specimen stages, using electron acclerating voltages up to 200 kV. Thin fragments were selected from the field of view and tilted until their diffraction patterns displayed sections of the reciprocal lattice which were recognizable as closely related to

known sections from the α-PbO_2 structure type. The symmetrical (100) section was particularly easy to recognize, and, because the b axis of the structures is known to be of almost constant length (*1*), the spacing of the 020 reflection ($d = 2.50$ Å) was used as a calibration. Thus, the size of the superlattice along c was determined from these patterns, and also the symmetry—whether centered or primitive. Approximate unit cell parameters thus determined from the electron diffraction patterns were used to confirm indexing of the X-ray powder data. Accurate parameters were then derived from the latter by a least-squares procedure.

4. Results

By means of the three complementary techniques of powder diffraction, selected area single-crystal electron diffraction, and single-crystal X-ray diffraction, the compounds listed in Table I have been characterized as members of the series $(Cr,Fe)_{2p}(Ti,Zr)_{p+2q}O_{5p+4q}$, with general compositions $pM_3O_5 \cdot qM_2O_4$. Their unit cells are approximated by the vectorial expressions, Eqs. (1), and it is evident that they are all intergrowths of the V_3O_5 and α-PbO_2 structure types, of which $CrFeTi_2O_7$ has provided the first example (*1*, *2*). Table I shows the remarkable constancy of the a, b and β unit cell parameters, and also the good agreement between the observed c parameters and those calculated from the data for the α-PbO_2 form of TiO_2 (*8*), using Eqs. (1).

In the following sections we describe the characterization of these phases in some detail, and give an account of the qualitative use of X-ray and electron diffraction intensity data as a means of confirming their structures.

4.1. Phase Characterization

A large number of closely spaced members of the intergrowth series can be obtained as a function of temperature over narrow composi-

TABLE I

CRYSTALLOGRAPHIC AND COMPOSITIONAL DATA FOR

Intergrowth $pM_3O_5 \cdot qM_2O_4$		Unit cell contents	Composition: x in MO_x	Monoclinic unit cell symmetry	c_{calcd} (Å)	Representative compound
p	q					
1	0	M_3O_5	1.667	Centred	13.66	$(Cr_{0.5}Fe_{0.5})_2\ Ti O_5$
4	1	$M_{14}O_{24}$	1.714	Prim.	32.78	$(Cr_{0.8}Fe_{0.2})_4\ Ti_3O_{12}$
3	1	$M_{11}O_{19}$	1.727	Centred	51.90	$(Cr_{0.8}Fe_{0.2})_6\ Ti_5O_{19}$
2	1	M_8O_{14}	1.750	Prim.	19.12	$Cr_2Ti_2O_7$
3	2	$M_{13}O_{23}$	1.769	Centred	62.82	$(Cr_{0.5}Fe_{0.5})_6\ Ti_7O_{23}$
4	3	$M_{18}O_{32}$	1.778	Prim	43.70	$(Cr_{0.8}Fe_{0.2})_4\ Ti_5O_{16}$
1	1	M_5O_9	1.800	Centred	24.59	$Fe_2\ Ti_3\ O_9$
3	4	$M_{17}O_{31}$	1.823	Prim.	84.71	$(Cr_{0.8}Fe_{0.2})_6(Ti_{0.8}Zr_{0.2})_{11}O_{31}$
2	3	$M_{12}O_{22}$	1.833	Prim	30.06	$(Cr_{0.8}Fe_{0.2})_2(Ti_{0.8}Zr_{0.2})_4O_{11}$
1	2	M_7O_{13}	1.857	Centred	35.52	$(Cr_{0.8}Fe_{0.2})_2(Ti_{0.8}Zr_{0.2})_5O_{13}$
2	5	$M_{16}O_{30}$	1.875	Prim.	41.00	$(Cr_{0.8}Fe_{0.2})_2(Ti_{0.8}Zr_{0.2})_6O_{15}$

tion ranges, and the preparation temperatures listed in Table I are those found by trial and error to produce essentially single phases at the appropriate composition. The difficulty of obtaining perfect single compounds in a multicomponent, quasicontinuous system is obvious, and the compounds listed in Table I should strictly be considered as having "average" compositions $MO_{x\pm\delta}$ centered on MO_x but with a composition distribution encompassing the infinite number of high order intergrowths possible in the range $\pm\delta$. The magnitude of δ will depend on variables such as the reaction time, temperature variation across the sample, rapidity of quenching, and microhomogeneity of the starting mixtures. By careful preparation of the samples we obtained products which gave X-ray powder reflections of a sharpness comparable with those of the KCl standard and which could all be indexed using unit cells derived from vectorial expressions (1). Each of the representative compounds listed in Table I was thus confirmed as an intergrowth of V_3O_5 and α-PbO_2 structure types. Typical indexed powder data are given in Table II.

Electron diffraction patterns proved to be a sensitive and reliable means for identifying or confirming any particular intergrowth, and several ($0kl$) reciprocal lattice sections from fragments of different compositions are shown in Fig. 3. The simple pseudohexagonal array of strong spots characteristic of both of the parent structures M_3O_5 and M_2O_4 is common to all the patterns, but there are in addition a number of weaker "superlattice" reflections. In some cases the subdivision of the c^* axis is obvious—for example, in Fig. 3(ii) it is clearly halved, and the symmetry remains centered, i.e., $k+l=2n$. However, in Fig. 3(iii) and (iv) many of the superlattice reflections are either very weak, or missing entirely, and the correct indexing of the patterns is not so obvious. Measurement of these patterns

INTERGROWTH COMPOUNDS $(Cr,Fe)_{2p}(Ti,Zr)_{p+2q}O_{5p+4q}$

Preparation	Unit Cell Parameters				Rutile CS
temp. °C	a, Å	b, Å	c, Å	β°	family
1500	7.007	5.018	14.011	137.90	(1 2 1)
1650	7.041	5.002	33.44	138.47	(4 9 5)
1500	7.019	4.994	52.83	138.57	(3 7 4)
1650	7.021	4.983	19.40	138.87	(2 5 3)
1200	7.042	4.991	63.99	138.82	(3 8 5)
1450	7.034	4.983	44.32	138.97	(4 11 7)
770	7.071	4.997	25.08	139.15	(1 3 2)
1500	7.082	4.996	85.93	138.87	(3 10 7)
1600	7.100	5.000	30.47	138.84	(2 7 5)
1600	7.116	5.007	36.03	138.93	(1 4 3)
1600	7.140	5.001	41.55	139.05	(2 9 7)

TABLE II

X-RAY POWDER DIFFRACTION DATA[a] FOR COMPOUNDS $(Cr,Fe)_{2p}(Ti,Zr)_{p+2q}O_{5p+4q}$

1. $(Cr_{0.8}Fe_{0.2})_4\ Ti_3O_{12}$

h	k	ℓ	$Sin^2\theta_{calcd}$	$Sin^2\theta_{obsd}$
0	0	5	0.03029	0.03015
-2	0	5	0.05336	0.05324
-2	1	7	0.07170	0.07178
0	1	7	0.08313	0.08291
0	2	0	0.09500	0.09523
-2	1	12	0.10059	0.10079
2	0	0	0.10931	0.10913
1	2	0	0.12232	0.12253
-3	1	12	0.13374	0.13391
-2	2	5	0.14836	0.14843
0	1	12	0.19827	0.19784
2	2	0	0.20430	0.20413
-4	1	12	0.22154	0.22134
-2	3	7	0.26169	0.26142
0	3	7	0.27312	0.27300
-2	3	12	0.29057	0.29051

2. $(Cr_{0.5}Fe_{0.5})_6\ Ti_7O_{23}$

h	k	ℓ	$Sin^2\theta_{calcd}$	$Sin^2\theta_{obsd}$
0	0	10	0.03355	0.03343
-2	0	10	0.05249	0.05246
-2	1	13	0.07195	0.07209
0	1	13	0.08056	0.08058
0	2	0	0.09544	0.09534
-2	1	23	0.10088	0.10094
2	0	0	0.11079	0.11060
1	2	0	0.12313	0.12328
-3	1	23	0.13374	0.13373
-2	2	10	0.14793	0.14781
0	1	23	0.20133	0.20091
2	2	0	0.20623	0.20597
-4	1	23	0.22200	0.22185
-2	3	13	0.26283	0.26296
0	3	13	0.27144	0.27114
-2	3	23	0.29176	0.29178

3. $(Cr_{0.8}Fe_{0.2})_6\ (Ti_{0.8}Zr_{0.2})_{11}O_{31}$

h	k	ℓ	$Sin^2\theta_{calcd}$	$Sin^2\theta_{obsd}$
0	0	14	0.03648	0.03654
-2	0	14	0.05079	0.05076
-2	1	17	0.07150	0.07185
0	1	17	0.07758	0.07774
0	2		0.09522	0.09523
-2	1	31	0.10130	0.10137
2	0	0	0.10956	0.10962
1	2	0	0.12261	0.12264
-1	1	31	0.12457	0.12471
-3	1	31	0.13281	0.13266
-2	2	14	0.14601	0.14583
0	1	31	0.20262	0.20245
2	2	0	0.20478	0.20483
-4	1	31	0.21910	0.21910

4. $(Cr_{0.8}Fe_{0.2})_2\ (Ti_{0.8}Zr_{0.2})_4O_{11}$

h	k	ℓ	$Sin^2\theta_{calcd}$	$Sin^2\theta_{obsd}$
0	0	5	0.03702	0.03683
-2	0	5	0.05033	0.05030
-2	1	6	0.07124	0.07160
0	1	6	0.07708	0.07704
0	2	0	0.09510	0.09503
-2	1	11	0.10134	0.10142
2	0	0	0.10907	0.10875
1	2	0	0.12237	0.12224
-3	1	11	0.13235	0.13231
-2	1	5	0.14543	0.14515
0	1	11	0.20293	0.20273
2	2	0	0.20417	0.20385
-2	3	0	0.26144	0.26173
0	3	6	0.26728	0.26712
-2	3	11	0.29154	0.29146

5. $(Cr_{0.8}Fe_{0.2})_2\ (Ti_{0.8}Zr_{0.2})_5\ O_{13}$

h	k	ℓ	$Sin^2\theta_{calcd}$	$Sin^2\theta_{obsd}$
0	0	6	0.03818	0.03782
-2	0	6	0.04977	0.04980
-2	1	7	0.07106	0.07128
0	1	7	0.07566	0.07542
0	2	0	0.09480	0.09467
-2	1	13	0.101116	0.10094
2	0	0	0.10875	0.10853
1	2	0	0.12200	0.12184
-1	1	13	0.12485	0.12460
-3	1	13	0.13184	0.13195
0	1	13	0.20292	0.20329
0	3	7	0.26527	0.26534
-2	2	13	0.29076	0.29083

6. $(Cr_{0.8}Fe_{0.2})_2\ (Ti_{0.8}Zr_{0.2})_6O_{15}$

h	k	ℓ	$Sin^2\theta_{calcd}$	$Sin^2\theta_{obsd}$
0	0	7	0.03936	0.3920
-2	0	7	0.04922	0.4908
0	1	6	0.05267	0.05261
0	0	9	0.06506	0.06491
-2	1	8	0.07089	0.7100
0	1	8	0.07516	0.07505
0	2	0	0.09502	0.09488
-2	1	15	0.101128	0.10121
2	0	0	0.10876	0.10896
1	2	0	0.12221	0.12224
-1	1	15	0.12568	0.12552
-3	1	15	0.13127	0.13142
-2	2	7	0.14423	0.14399
0	3	8	0.26519	0.26519
-2	3	15	0.29131	0.29130

[a] Cu$K\alpha$, radiation, KCl internal standard $a = 6.2931$ Å.

shows that the spacing between adjacent superlattice spots is one-fifth and one-seventh of the subcell spacing in Fig. 3(iii) and (iv), respectively, and that in both cases the symmetry is primitive.

While electron diffraction patterns from any single fragment in a preparation defined by X-ray powder data as a single phase were in general very sharp, as shown in Fig. 3, indicating both homogeneity and long-range order, small but specific variations in the details of the

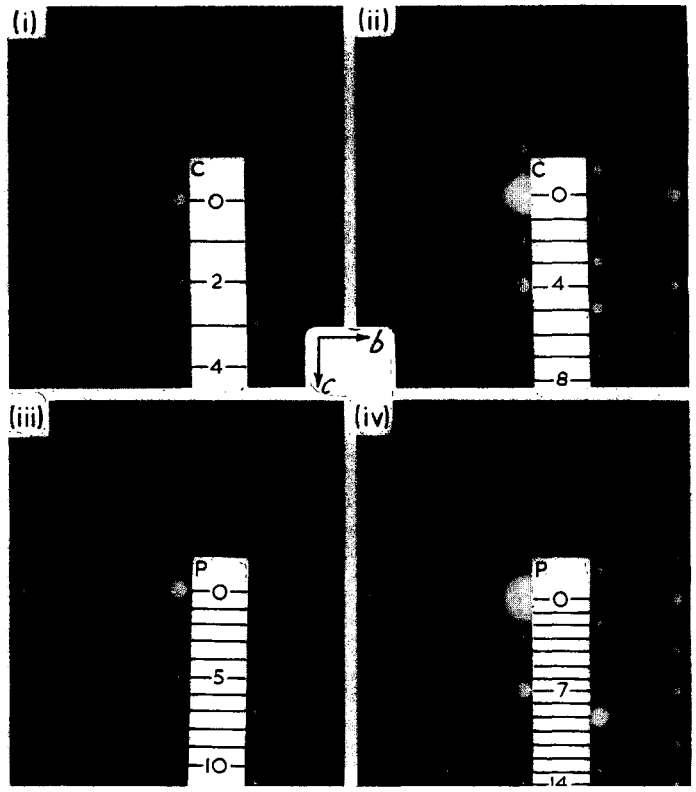

FIG. 3. 0*kl* electron diffraction patterns from thin fragments with the compositions (i) $(Cr_{0.5}Fe_{0.5})_2TiO_5$; (ii) $(Cr_{0.85}Fe_{0.15})_2Ti_3O_9$; (iii) $(Cr_{0.8}Fe_{0.2})_4Ti_3O_{12}$; (iv) $(Cr_{0.8}Fe_{0.2})_4Ti_5O_{16}$.

superlattice were often found in different fragments from the same preparation. It appears that these differences can be attributed to minute variations in composition between crystallites in the polycrystalline sintered preparations, but that within any particular crystallite a highly ordered structure is obtained. These compositional variations, i.e., $MO_{x\pm\delta}$, are accommodated by the formation of high order intergrowths P_pQ_q, in which the values of p and q may be very large. The electron diffraction patterns for such high order intergrowths are very similar to those for the simpler intergrowths, shown in Table I and Fig. 4, usually having the same number of superlattice reflections with the same relative intensities. The patterns differ only in the slight displacements of the spot positions along c^*, resulting in apparent "spacing anomalies." This is discussed in more detail below.

4.2. Confirmation of Structures

For the compounds $(Cr,Fe)_{2p}(Ti,Zr)_{p+2q}O_{5p+4q}$ listed in Table I the observed unit cell data are consistent with their formulation as intergrowths of V_3O_5 and α-PbO_2 structure types, i.e., $pM_3O_5 \cdot qM_2O_4$, or P_pQ_q. However, for all but the simplest intergrowths the ordering sequence of P and Q slabs is not uniquely determined by the unit cell parameters alone, and single-crystal X-ray intensity data are required to establish the detailed structures. In particular, the calculated intensities of the 00*l* superlattice reflections will be very sensitive to the ordering sequence chosen.

We have obtained single-crystal X-ray data for the phases M_8O_{14} (P_2Q) (*2*), $M_{11}O_{19}$ (P_3Q) and $M_{16}O_{30}$ (P_2Q_5), and although refinement of the data for the latter two compounds is still in progress the initial results show that there is a *maximum alternation* of P and Q slabs, so that for $M_{16}O_{30}$ for example the ordering sequence is PQQPQPQQP. For these three compounds it was observed that the relative intensities of the "order sensitive" 00*l* reflections in electron diffraction patterns from thin fragments were qualitatively the same as those in the X-ray

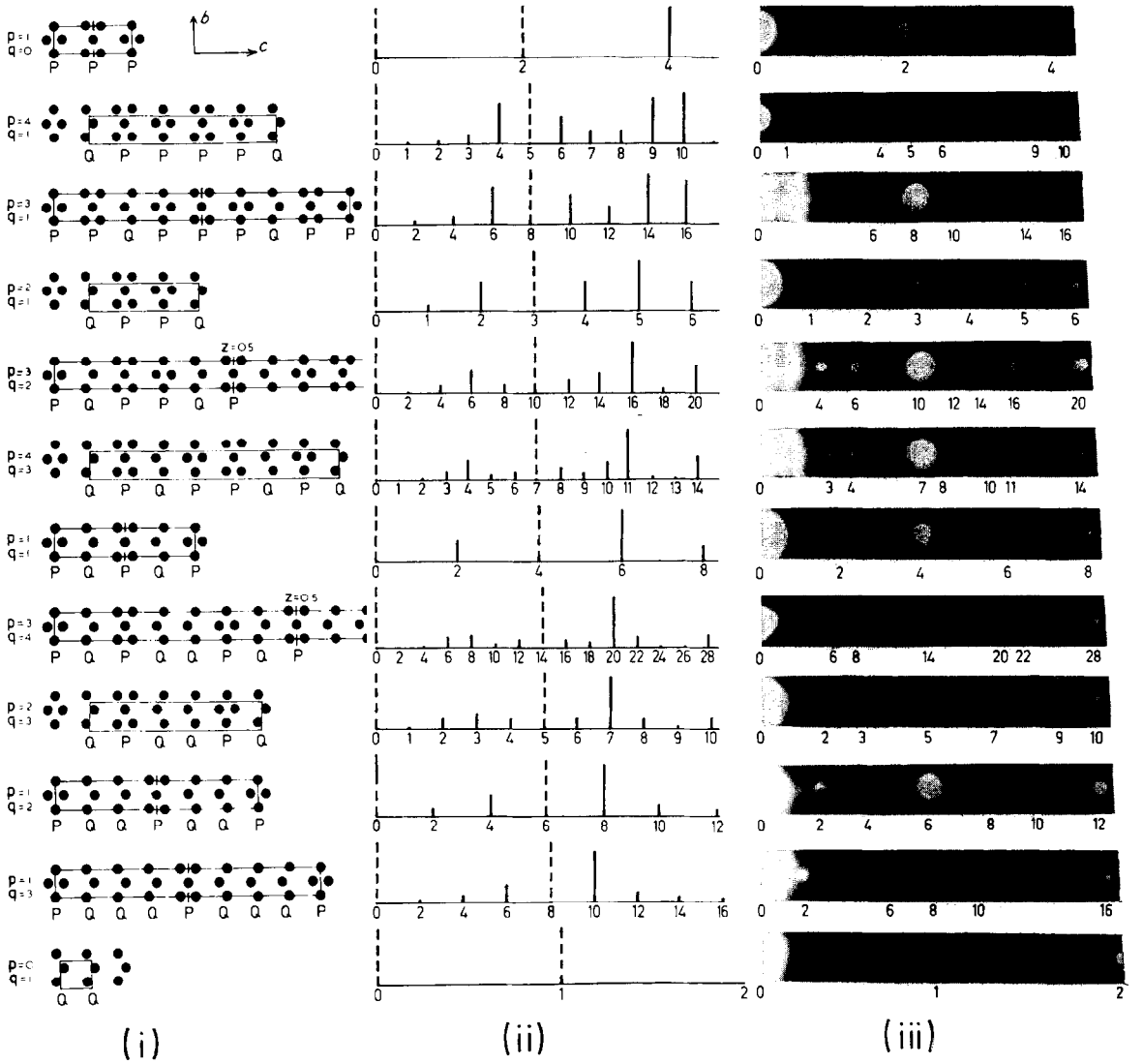

FIG. 4. Structural models and diffraction data for the intergrowths listed in Table I. (i) Idealized models of intergrowths P_pQ_q (P = M_3O_5, Q = M_2O_4), showing only the positions of metal atoms in the plane $x = 0$. In some cases where the symmetry is centered (odd values of p) the unit cell is not complete beyond $x = 0.5$. Slabs of the V_3O_5 and α-PbO_2 structure types are identified by the letters P and Q, respectively. (ii) Calculated 00l diffraction intensities for the models in 4i. The horizontal scale is proportional to $1/d$. The numbers give the l indices of the reflections. The broken lines are subcell reflections which are always very strong and are not drawn to scale. (iii) 00l electron diffraction data from thin fragments with compositions corresponding to those of the models in (i). The l indices of the stronger reflections are shown, and the horizontal scale is the same as in (ii).

single-crystal patterns, despite the fact that the interactions between an electron beam and a crystal are severely dynamical (*12*). This qualitative correspondence prompted us to attempt a confirmation of the *maximum alternation* structural model from electron diffraction data. Even without extensive calculations one might expect to achieve correlation between calculated and observed strong, weak and absent reflections.

The following simple procedure was used. The maximum alternation structures were all idealized as shown in Fig. 1, and the oxygen atoms, which in the ideal case do not contribute to superlattice reflections, were ignored entirely. The arrangements of metal atoms were taken to be as shown in Fig. 4(i), and their scattering factors were assumed to be equal, and independent of θ. Structure factors for 00l reflections were then

calculated, and the results were squared and plotted as vertical lines whose length represents intensity (Fig. 4(ii)). The horizontal scale is linear in d^* (d = interplanar spacing), and the numbers indicate the value of l. The 000 and the first subcell reflections are drawn as broken lines, since their intensities were always very much higher than those of the remaining reflections, and could not conveniently be plotted on the same scale.

Experimental 00l electron diffraction patterns, enlarged to the same d^* scale, are shown in Fig. 4 (iii). It is seen that for all the intergrowths shown in Fig. 4, the calculations based on the "maximum alternation" model correctly reproduce the order of intensities for neighboring 00l reflections. For example, in the case $p = 4$, $q = 3$ the prediction is that strong spots will occur for $l = 4$, 7, 11 and 14 and that those for $l = 2$, 5, 6, 9, 12 and 13 will be weak. Similarly, for $p = 3$, $q = 4$, $l = 6$, 8, 14, 20, 22 and 28 should have reasonable intensity, and the remainder should be weak or absent. The observed patterns are seen to display these sequences. The intensity agreement is far from quantitative, but is not unreasonable in view of the limitations of the model and the neglect of dynamical effects. The most obvious discrepancy between calculated and observed intensities occurs for the second subcell reflection, i.e., the last on the right in the patterns shown in Fig. 4. This is due to the neglect of the oxygen atoms and to the idealization of the metal atom positions.

The strength of this qualitative approach is best seen by comparing the relative intensities calculated for the *maximum alternation* model with those calculated for other alternative models which are also compatible with the unit cell data. For example, the calculated intensities for the three possible sequences with the overall composition P_4Q_3 are shown in Fig. 5. Only the first of these sequences, in which there is maximum alternation of P and Q slabs, gives reasonable agreement with the observed data, and the remaining possibilities can be rejected immediately.

4.3. High Order Intergrowths

The electron diffraction sections shown in Fig. 4(iii) were obtained from fragments taken from the "single phase" preparations of the compounds listed in Table I. Each of these preparations actually spans a small range of compositions, and contains a very large number of high order intergrowth phases. Almost invariably the electron diffraction patterns contain spacing anomalies which in fact correspond to high order intergrowths.

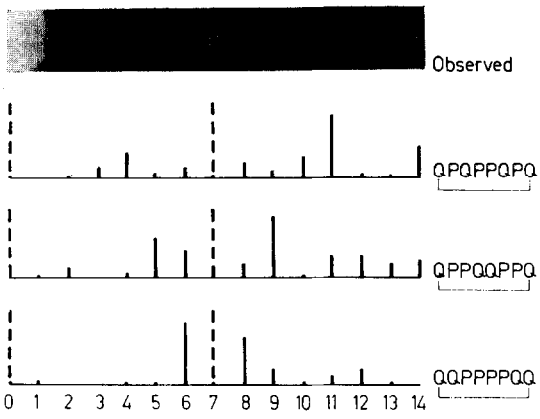

FIG. 5. Comparison of observed 00l electron diffraction data (top) from a fragment of composition $(Cr_{0.8}Fe_{0.2})_4Ti_5O_{16}$, i.e., P_4Q_3, with calculated intensities for three possible structural models, each of which has the same composition, symmetry, and unit cell dimensions and differs only in the sequence of slabs of V_3O_5 (P) and α-PbO_2 (Q) structure types. Only the first sequence, in which there is a *maximum alternation* of P and Q slabs, gives satisfactory agreement with the observed data.

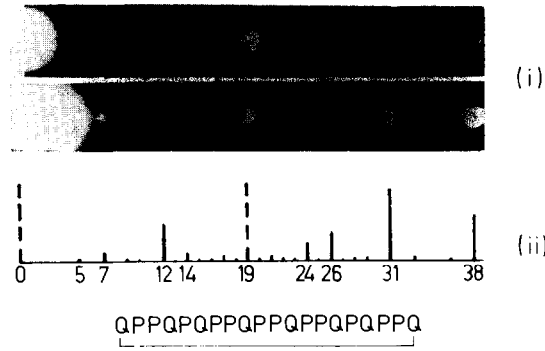

FIG. 6(i). 00l electron diffraction data from two different fragments of nominal composition $Cr_2Ti_2O_7$, i.e., P_2Q, showing equally spaced spots characteristic of the exact PQ_2 intergrowth (top), and small splittings of the superlattice spots (lower) which correspond to a spacing anomaly. (ii) Calculated 00l diffraction pattern for the high order intergrowth $P_{12}Q_7$, having the maximum alternation sequence, showing a likely explanation for the spacing anomaly. All the spots in the observed lower pattern are reproduced as relatively intense lines in the calculated pattern, and the remainder have small or negligible intensity.

The exact periodicity of any particular intergrowth requires careful measurement of the spot positions. An obvious example of a high order intergrowth is seen in the pattern in Fig. 6, where there are two quite distinct and apparently unrelated spacings between adjacent spots along the 00l row. Measurements of the positions of both the 00l and 01l spots were made with a traveling microscope, and it was found that they could be fitted by a common primitive superlattice with a c axis dimension of 121 Å. This cell gives the indices 00 19 to the first subcell spot in Fig. 6, and of course most of the possible 00l reflections have negligible intensity. The nominal composition of the sample from which the pattern was recorded was P_2Q, and we must therefore find values of p and q with the following constraints: $p \simeq 2q$, to satisfy the composition; p even, since the symmetry is primitive and $5p + 4q = 4(c/b)$, from (1).

The combination $p = 12$, $q = 7$ satisfies these criteria, and the calculated value of c is 120.3 Å. The calculated 00l intensities for the maximum alternation version of the $P_{12}Q_7$ intergrowth are shown in Fig. 6, and they reproduce the observed data satisfactorily. The composition of the intergrowth, $12M_3O_5 \cdot 7M_2O_4 = M_{50}O_{88} = M_{1.760}$ differs from the nominal value of $2M_3O_5 \cdot M_2O_4 = M_8O_{14} = MO_{1.750}$; this difference probably indicates failure to attain equilibrium over the whole sample. A more subtle example is the case $p = 3$, $q = 4$ in Fig. 4. Careful measurement of the observed data for a particular fragment indicates a true unit cell with $c = 399$ Å, having the composition $p = 28$, $q = 37$, i.e., $MO_{1.822}$, rather than $p = 3$, $q = 4$, i.e., $MO_{1.824}$. The computed intensity distribution was virtually the same as that shown in Fig. 4(ii).

The identification of high order intergrowths by electron diffraction suggests that in this series of

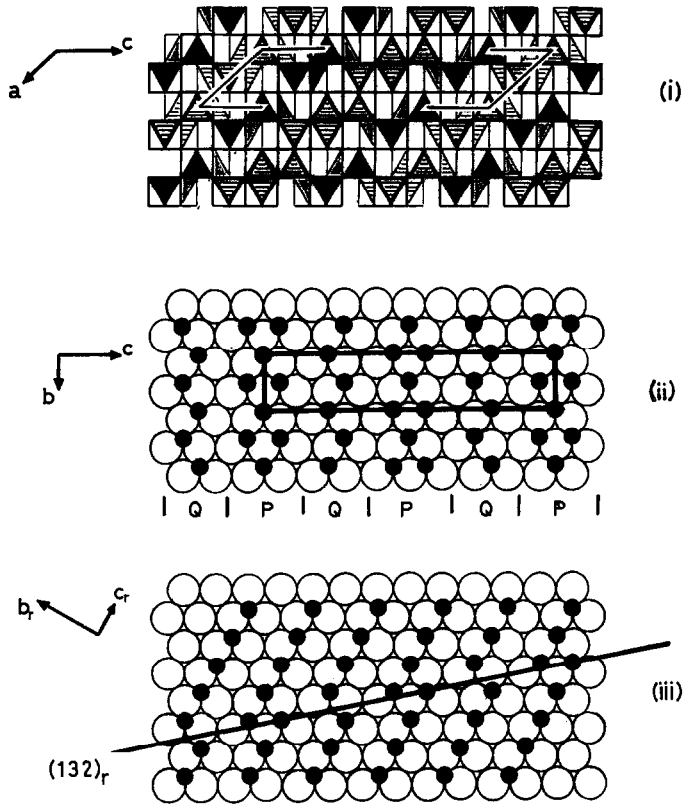

FIG. 7. Maximum alternation model for the structure of the intergrowth compound $M_3O_5 \cdot M_2O_4$, i.e. PQ. (i) Projection of the idealized structure viewed down [010]. (ii) (100) section through the idealized structure. (iii) Result of the operation $\frac{1}{2}[0\bar{1}1](132)_r$ on the rutile structure; repetition of this CS operation at 5 Å intervals generates the structure shown in (ii) and adopted by $Fe_2Ti_3O_9$ (Table I).

compounds the tendency to achieve long-range order within a single-crystal grain is very strong. The fact that the samples tend to be inhomogeneous from grain to grain, at the level detectable with electrons, probably implies that intercrystalline diffusion between grains in the polycrystalline sintered matrix is very slow compared with times required to establish order within individual grains.

5. Discussion

The evidence presented in this paper indicates that for suitable Cr:Fe and Ti:Zr ratios in the system $(Cr,Fe)_2O_3$–$(Ti,Zr)O_2$ the composition range $MO_{1.667}$–MO_2 is spanned by a quasi-continuous series of ordered intergrowths of the V_3O_5 and α-PbO_2 structural types, $pM_3O_5 \cdot qM_2O_4$. The series cannot be considered as a solid solution because of the completely discontinuous change in the c axis with composition and the ordered nature of any particular P_pQ_q intergrowth. The region of apparent solid solubility for compositions near $Cr_2O_3 \cdot 2TiO_2$ in the Cr_2O_3–TiO_2 system (*13*) is a particular case of the series of compounds described in the present work. A comparable continuous series of ordered phases has been identified by Roth and Stephenson in the Ta_2O_5–WO_3 system (*14*). Indeed, many regions of phase diagrams earlier labeled as solid solution single phase regions in the classical sense, under close scrutiny turn out to contain large numbers of completely ordered structures.

The V_3O_5 structure type is defined by $p = 1$, $q = 0$ and, as the ratio of q/p tends to finite values, oxidation of M_3O_5 (or substitution of M^{4+} for M^{3+} in $M_2^{3+}M^{4+}O_5$) can be considered to introduce in the M_3O_5 host lattice, distantly spaced slabs of α-PbO_2 structure type. Progressive "oxidation" increases the number of M_2O_4 slabs to values comparable with the number of M_3O_5 slabs. The structural evidence indicates that in the intergrowth structures the repetition width of either type of segment is as small as the net composition will allow. This

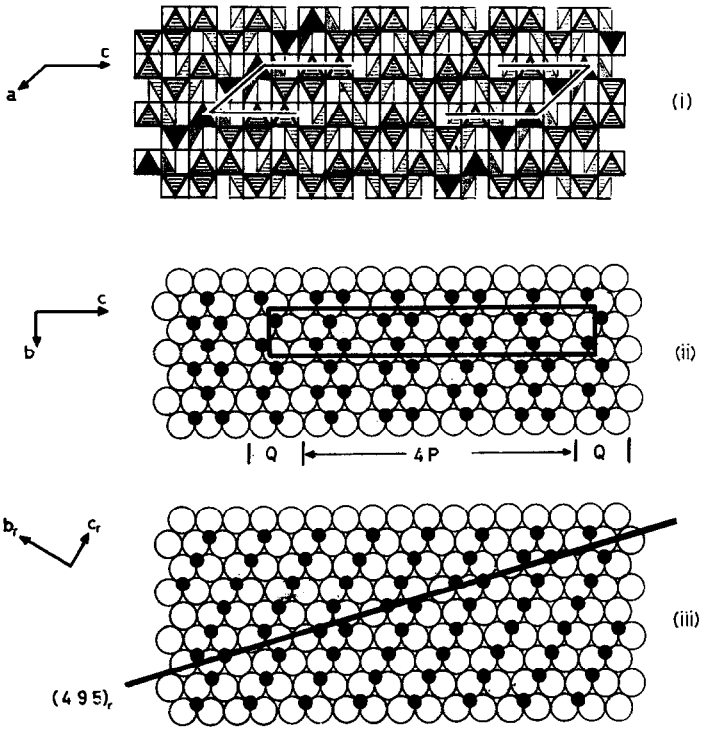

FIG. 8. Maximum alternation model for the structure of the intergrowth compound $4M_3O_5 \cdot M_2O_4$, i.e., P_4Q. (i) Projection of the idealized structure viewed down [010]. (ii) (100) section through the idealized structure. (iii) Result of the operation $\frac{1}{2}[0\bar{1}1](495)_r$ on the rutile structure; repetition of this CS operation at 5 Å intervals generates the structure shown in (ii) and adopted by $(Cr_{0.8}Fe_{0.2})_4Ti_3O_{12}$ for example (see Table I).

"*maximum alternation*" effect has as its physical consequence a maximally uniform distribution of "oxidized" segments through the structure and a minimal extension of the M_3O_5 segments containing face-shared octahedra. Thus there is a maximum dilution of the regions of strongest ion–ion interaction. As q rises towards large values and p becomes small, "slightly reduced" α-PbO_2 structure type, with widely separated segments of V_3O_5 type, is defined.

The description of the phases with formula $(Cr,Fe)_{2p}(Ti,Zr)_{p+2q}O_{5p+4q}$ as intergrowths of the V_3O_5 and α-PbO_2 structural types is a powerful one, and allows the structures to be easily visualized. Their unit cells, as for those of the V_3O_5 and α-PbO_2 types, have a 5 Å axis which is one of the major repeat distances for hexagonally close packed oxygen layers. In the intergrowth phases the M_3O_5 and M_2O_4 slabs, infinite in two dimensions, contain this axis, and the complete structures may be viewed in projection down it, as shown in Figs. 7–9.

An alternative representation of the compounds $(Cr,Fe)_{2p}(Ti,Zr)_{p+2q}O_{5p+4q}$ can be based on shear in the rutile structure, Figs. 1 and 7–9. Although this has the disadvantage that the three-dimensional shear planes are difficult to visualize, the description of the phases as belonging to "swinging shear" rutile CS families does provide a basis for correlation with a number of other series of compounds such as V_nO_{2n-1} (*15*) and Ti_nO_{2n-1} (*16*), $3 \leqslant n \leqslant 10$, and the "swinging shear" structures occurring at the titanium-rich end of the Ti–Cr–O system (*5*). It is also easy to postulate mechanisms for compositional changes in the system in terms of a swinging of the direction of shear planes whose spacing remains constant, as recently described by Bursill and Hyde (*17*) and by Allpress (*18*) for the case of ReO_3-type CS structures.

As an example of the CS representation, consider the simplest possible intergrowth, $p = 1$ and $q = 1$, for which the rutile CS plane is given by

$$(hkl)_r = (121) + (011) = (132).$$

Figure 7(iii) shows a $(100)_r$ section through the rutile structure, which a $(132)_r$ plane intersects

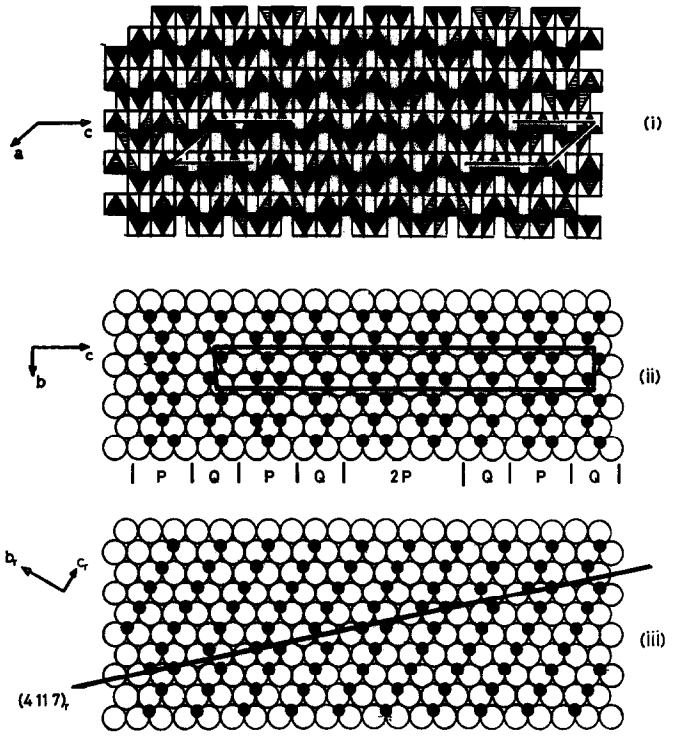

FIG. 9. Maximum alternation model for the structure of the intergrowth compound $4M_3O_5 \cdot 3M_2O_4$, i.e., P_4Q_3. (i) Projection of the idealized structure viewed down [010]. (ii) (100) section through the idealized structure. (iii) Result of the operation $\frac{1}{2}[0\bar{1}1](4\ 11\ 7)_r$ on the rutile structure; repetition of this CS operation at 5 Å intervals generates the structure shown in (ii) and adopted by $(Cr_{0.8}Fe_{0.2})_4Ti_5O_{16}$ for example (see Table I).

in the line $[0\bar{2}3]_r$. The result of the CS operation $\frac{1}{2}[0\bar{1}1](132)_r$ is seen to introduce sections of V_3O_5 (P) and α-PbO_2 (Q) type structures in the sequence P Q P Q... along the CS plane direction. It is easy to see that repetition of the operation on successive $(132)_r$ planes, separated by 5 Å, i.e., $\frac{1}{2}[013]_r$, reproduces the structure shown in Fig. 7ii, that of $(Cr,Fe)_2Ti_3O_9$. Similarly, CS on $(495)_r$, and $(4\ 11\ 7)_r$ is shown in Figs. 8(iii) and 9(iii). Repeated shear on these rutile planes, at fixed intervals of $\frac{1}{2}[013]_r$, gives the structures adopted by $(Cr,Fe)_6(Ti,Zr)_5O_{11}$ and $(Cr,Fe)_8(Ti,Zr)_{10}O_{32}$. In Table I are given the CS planes by which the various $(Cr,Fe)_{2p}(Ti,Zr)_{p+2q}O_{5p+4q}$ phases may be derived from the rutile structure. It appears fundamental to this representation that only for the case of maximum alternation of the (121) and (011) rutile shear segments does the shear plane operation produce the same structure as the vector addition of the individual shear or APB operations.

In the classification scheme of Bursill *et al.* (*5*), each rutile shear plane defines a *family* of rutile CS structures in which each member differs from the other by having a different shear plane spacing. In this classification, each of the V_3O_5–α-PbO_2 intergrowths is an end member of a *different* rutile CS family.

The equivalence of the two representations which we have presented emphasizes that structural features or crystal-chemical properties not evident in a particular representation may well be evident in another, and that as varied an approach as possible should be made to the description and understanding of any series of structurally related phases.

References

1. I. E. Grey and A. F. Reid, *J. Solid State Chem.* **1**, 576 (1970).
2. I. E. Grey and W. G. Mumme, *J. Solid State Chem.* **5**, 168 (1972).
3. A. I. Zaslevskij and S. S. Tolkacev, *Zh. Fiz. Khim.* **26**, 743 (1952).
4. S. Asbrink, S. Friberg, A. Magneli, and G. Andersson, *Acta Chem. Scand.* **13**, 604 (1959).
5. L. A. Bursill, B. G. Hyde, and D. K. Philp, *Phil. Mag.* **23**, 1501 (1971).
6. S. Andersson and J. Galy, *J. Solid State Chem.* **1**, 576 (1970).
7. H. Horiuchi, M. Tokonami, N. Morimoto, K. Nagasawa, Y. Bando, and T. Takada, *Mater. Res. Bull.* **6**, 833 (1971).
8. R. G. McQueen, J. C. Jamieson, and S. P. Marsh, *Science* **155**, 1404 (1967).
9. S. Andersson, A. Sunholm, and A. Magneli, *Acta Chem. Scand.* **13**, 989 (1959).
10. L. Pauling, *Z. Kristallogr. Kristallgeometrie Kristallphys. Kristallchem.* **73**, 97 (1930).
11. J. Spyridelis, D. Delavignette, and S. Amelincky, *Phys. Status Solidi* **19**, 683 (1967).
12. J. M. Cowley, *Progr. Mater. Sci.* **13**, 267 (1967).
13. O. W. Flörke and C. W. Lee, *J. Solid State Chem.* **1**, 445 (1970).
14. R. S. Roth and N. C. Stephenson, *in* "The Chemistry of Extended Defects in Nonmetallic Solids" (L. Eyring and M. O'Keeffe, Eds.). North-Holland, Amsterdam (1969).
15. G. Andersson, *Acta Chem. Scand.* **8**, 1599 (1954).
16. S. Andersson, B. Collen, U. Kuylenstierna, and A. Magneli, *Acta Chem. Scand.* **11**, 1641 (1957).
17. L. A. Bursill and B. G. Hyde, *J. Solid State Chem.* **4**, 430 (1972).
18. J. G. Allpress, *J. Solid State Chem.* **4**, 173 (1972).